

# JGR Space Physics

## RESEARCH ARTICLE

10.1029/2022JA031262

### Key Points:

- Intensification (weakening) of equatorial plasma bubble (EPB) is observed by GOLD during the initial (recovery) phase of a storm
- Storm-origin electric fields considerably altered the pre-reversal electric field and influenced EPB development
- Both observations and simulations confirm that disturbance electric fields modified the plasma distribution and instability growth rate

### Supporting Information:

Supporting Information may be found in the online version of this article.

### Correspondence to:

B. C. Amadi,  
[amadibrians@gmail.com](mailto:amadibrians@gmail.com)

### Citation:

Amadi, B. C., Qian, L., de Paula, E. R., McInerney, J. M., Kherani, E. A., Santos, A. M., & Sanchez, S. A. (2023). Intensification and weakening of equatorial plasma bubble development observed by GOLD during different phases of a geomagnetic storm. *Journal of Geophysical Research: Space Physics*, 128, e2022JA031262. <https://doi.org/10.1029/2022JA031262>

Received 22 DEC 2022  
 Accepted 6 SEP 2023

## Intensification and Weakening of Equatorial Plasma Bubble Development Observed by GOLD During Different Phases of a Geomagnetic Storm

B. C. Amadi<sup>1</sup> , L. Qian<sup>2</sup> , E. R. de Paula<sup>1</sup> , J. M. McInerney<sup>2</sup>, E. A. Kherani<sup>1</sup> , A. M. Santos<sup>1,3</sup> , and S. A. Sanchez<sup>1</sup> 

<sup>1</sup>Instituto Nacional de Pesquisas Espaciais (INPE), Sao Jose dos Campos, SP, Brazil, <sup>2</sup>National Center for Atmospheric Research (NCAR), Boulder, CO, USA, <sup>3</sup>State Key Laboratory of Space Weather, NSSC/CAS, Beijing, China

**Abstract** Equatorial plasma bubble (EPB) development during different phases of the geomagnetic storm of 3–4 November 2021 ( $SYM H_{\min} = -118$  nT) was examined using observations and simulations. The initial phase of the storm coincided with postsunset (about 30 min after sunset) at Fortaleza (FZ) and São Luís (SL) with longitudes of  $\sim 38.45^\circ\text{W}$  and  $\sim 44^\circ\text{W}$  respectively on November 3 while the recovery phase of the storm started at 12:45 UT on November 4. GOLD shows the longest (shortest) extension of EPBs on November 3 (4) compared to days before and after November 3 and 4, including quiet days. This indicates an intensification (weakening) of EPBs on November 3 (4). From ionosondes at FZ and SL, a strong (weak) range spread F (SSF (RSF)) was observed on November 3 (4). The postsunset peak F layer height on November 3 reached 450 km and exceeded the preceding and succeeding days by  $\sim 50$ – $100$  km at SL indicating the presence of a Prompt Penetration Electric Field (PPEF) which enhanced EPB development via the favorable postsunset vertical  $\mathbf{E} \times \mathbf{B}$  and Rayleigh-Taylor instability (RTI) mechanisms on November 3. The lower-than-quiet time F layer height observed on November 4 during Pre-reversal enhancement (PRE) indicates the presence of a westward-oriented Disturbance Dynamo Electric Field (DDEF) that undermined RTI growth and led to the weakening of EPB development. Simulation results confirm that the storm-time electric fields modified the evening-time ionosphere and influenced the magnitude of vertical  $\mathbf{E} \times \mathbf{B}$  drift required for the development of EPBs.

## 1. Introduction

Equatorial plasma bubbles (EPBs) are magnetic field-aligned irregularities observed in the equatorial ionosphere. They are characterized by three-dimensional plasma density depletions, scale sizes that range from several hundreds to thousands of kilometers in the magnetic meridional direction and tens to hundreds of kilometers in the zonal direction (Bhattacharyya, 2022; Kil, 2015). The EPBs develop from the bottomside ( $\sim 200$  km) of the F region and can extend to an altitude of  $\sim 2,600$  km (Sousasantos et al., 2023), mostly occurring between the post-sunset and presunrise time frames, and drifts from the postsunset to the midnight/presunrise sectors with a speed that ranges from 20 to 190 m/s (de Paula et al., 2002, 2019; Karan et al., 2020) but can drift westward during geomagnetically disturbed conditions (Abdu et al., 2003). EPBs manifest as spread on ionogram traces generally known as Equatorial Spread F (ESF).

The development of EPBs depends on the growth rate of Rayleigh-Taylor Instability (RTI) which is greatly influenced by the  $\mathbf{E} \times \mathbf{B}$  drift; orchestrated by the interplay between the zonal electric field ( $\mathbf{E}$ ) and horizontally oriented magnetic field ( $\mathbf{B}$ ). The occurrence of EPBs in the postsunset period is associated with the enhancement of the neutral wind dynamo eastward-oriented  $\mathbf{E}$  prior to a westward turn at nighttime (J. V. Eccles, 1998; J. Eccles et al., 2015; Farley et al., 1986; Fesen et al., 2000; Haerendel & Eccles, 1992; Kelley, 2009; Richmond & Fang, 2015). This is known as Pre-reversal Enhancement (PRE) and results in an uplift of the F layer, an increase in the height-dependent density gradient, and positive growth of RTI, hence possible development of EPBs (Abdu, 2001; Alam Kherani et al., 2004; Kil, 2015; Sultan, 1996).

Factors that influence RTI growth rate are subject to modification during geomagnetic storms owing to the energy input into the upper atmosphere at high latitudes and global impact. The rapid change in polar cap potential due to the southward turning of the north-south component ( $B_z$ ) of the Interplanetary Magnetic Field (IMF) can cause the magnetospheric convection electric field (MCE) to overwhelm the shielding electric field (SEF) provided by the ring current polarization electric field (Klimenko & Klimenko, 2012; Wei et al., 2015). The

excess of this field (MCE) can penetrate instantly to the low-latitude ionosphere, and this is known as a Prompt Penetration Electric Field (PPEF). Disturbed neutral winds during geomagnetic storms can also alter low-latitude electric fields through a neutral wind dynamo process causing a Disturbance Dynamo Electric Field (DDEF). A daytime PPEF enhances an eastward electric field (Abdu, 1997, 2012; Fejer et al., 2008; Martinis et al., 2005) while DDEF is associated with a westward electric field, Joule heating, enhancement of precipitation especially around the South Atlantic Magnetic Anomaly (SAMA), generation of traveling ionospheric disturbances (TIDs), and change of atmospheric chemistry (Hashimoto et al., 2020; Hocke & Schlegel, 1996; Lissa et al., 2020; Qian et al., 2019; Xiong et al., 2016).

The response of EPB development to geomagnetic storms has been widely investigated using different techniques including the use of ionosondes (Abdu et al., 2003; Santos et al., 2012; Sripathi et al., 2018), TEC derived from the Global Navigation Satellite Systems (GNSS) (Cherniak et al., 2019; de Paula et al., 2019; F. Huang et al., 2021; Picanço et al., 2022), low-earth orbiting (LEO) satellites (Chang et al., 2022; Wan et al., 2022; Zakharenkova et al., 2019), ground- and space-based imagers (Ghodpage et al., 2018; Karan et al., 2023; Wu et al., 2020) and numerical models (Bhattacharyya et al., 2019; Blanc & Richmond, 1980; Carter et al., 2014, 2016). Four important deductions from these studies are (a) The influence of disturbance electric fields on ESF/EPB development is a function of local time. That is, the onset time of the storm can pivot the enhancement, suppression, or disruption of ESF/EPB development, (b) Disturbance electric fields due to a given storm can persist from the onset of a storm to up to a few days, (c) The polarity of the disturbance field is modulated by the direction of  $B_z$ . Thus, PPEF (and DDEF) can switch from east to west (and vice versa) depending on the state of  $B_z$  and (d) One of the paths via which these disturbance fields influence EPB/ESF development is the redistribution of plasma that either enhances or undermines the RTI growth rate.

On 1 November 2021, the sun emitted two C and one M class flares with an average time interval of 2.5 hr between emissions. Each flare was succeeded by a Coronal Mass Ejection (CME) traveling toward Earth and caused a geomagnetic storm that extended from the 3rd to the 4th of November 2021; the most severe storm of 2021. During the main phase of this storm, the equatorial electrojet was oriented westward; a phenomenon known as a Counter Equatorial Electrojet (CEJ), and had geomagnetic indices with some similarities to the intense St Patrick's day storm of 2015. The initial phase of this storm occurred at about postsunset of November 3 while a section of the recovery phase coincided with postsunset on November 4 in NASA's Global-scale Observation of the Limb and Disk (GOLD) field of view (FOV). This presents an ample opportunity to investigate the development of EPBs during different phases of a storm that coincided with PRE on two consecutive days, in the same season (high ESF occurrence season), and under similar solar conditions.

Studies such as this are important for the complete understanding of the onset conditions of EPBs/ESF toward accurate EPB prediction, planning of space missions, specifications for space-based systems, and engineering robust technological systems that can withstand the scintillation effects of EPBs/ESF. This study will utilize observations of GOLD, ionosondes, and results from the National Center for Atmospheric Research (NCAR) Whole Atmosphere Climate Community Model with Ionosphere and Thermosphere eXtension (WACCM-X) model to investigate the development of EPBs/ESF during the storm of 3–4 November 2021. The two-dimensional (2D) synoptic view of GOLD provides 2D evolution of EPBs, whereas the WACCM-X model can provide descriptions of the storm-disturbance electric fields during the initial and recovery phases, and thus explain the intensification and weakening of EPBs at postsunset on November 3 and 4 within GOLD's FOV.

## 2. Experimental Data and Model

### 2.1. Geomagnetic Data

Geomagnetic data utilized in this study include the north-south component ( $B_z$ ) of the Interplanetary Magnetic Field (IMF), the Interplanetary east-west electric field ( $E_y$ ), solar wind speed ( $V_{sw}$ ), symmetric-H (SYM-H), and the geomagnetic Kp index. All parameters but Kp index have a 1-min resolution and were accessed via NASA's website: [https://omniweb.gsfc.nasa.gov/form/omni\\_min.html](https://omniweb.gsfc.nasa.gov/form/omni_min.html).

### 2.2. GOLD Data

To visualize EPBs over the South American sector, nighttime OI 135.6 nm emissions measured by GOLD was utilized. GOLD is one of NASA's space missions onboard a geostationary satellite at 35,786 km altitude and

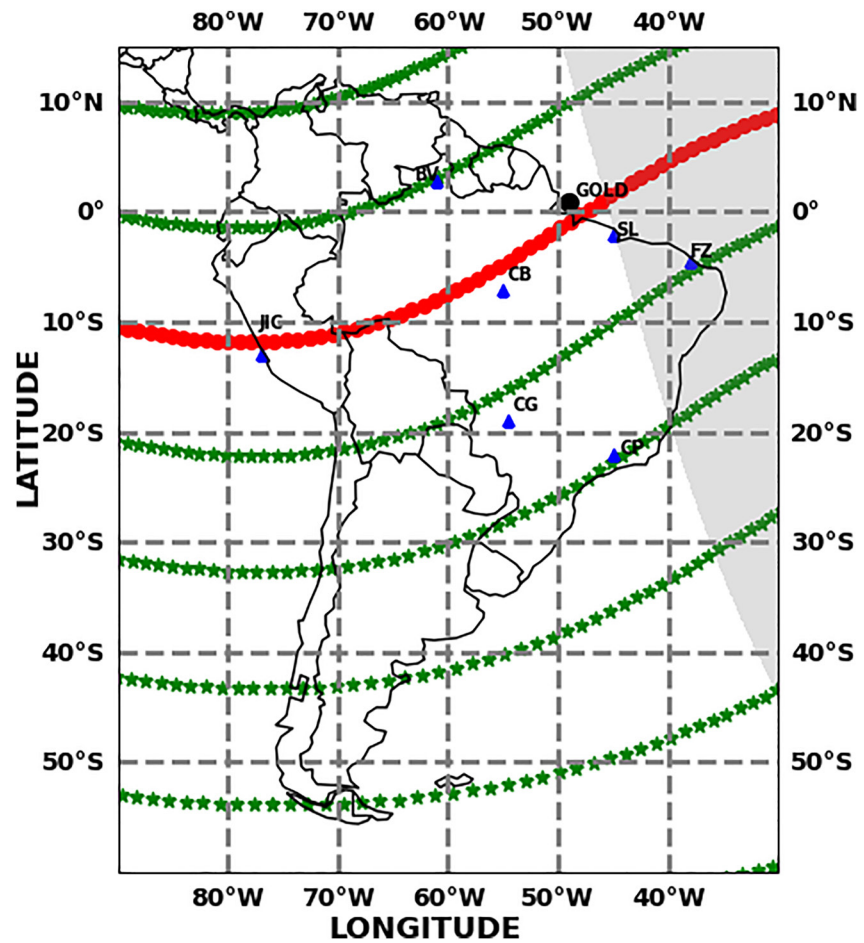


**Figure 1.** Map showing the geographic locations of GOLD (filled black circle), digisonde stations at São Luís (SL), Fortaleza (FZ), Boa Vista (BV), Cachimbo (CB), Campo Grande (CG), Cachoeira Paulista (CP) and Jicarica (JIC) (filled blue triangles). The red line is the magnetic equator and the green lines are magnetic latitudes. Only digisonde data adjacent to the magnetic equator are utilized in this study. The line demarcating the gray (nightside) and white (dayside) backgrounds is the solar terminator (ST) at 21:00 UT (~18:00 LT) on 3 November 2021.

47.5°W longitude. It scans the atmosphere from the African sector across the Atlantic to the American sector in nighttime mode and its position in geostationary orbit ensures a wide field of view over the equatorial and adjacent regions and an ability to observe the same longitudinal location every night (Eastes et al., 2017, 2020). These repeated measurements allow GOLD to distinguish between spatial and temporal variations in the evolution and characteristics of equatorial irregularities including EPBs and EIAs (Eastes et al., 2017) thus making GOLD data suitable for this study. GOLD observes the Earth's far ultraviolet (FUV) airglow at ~134–162 nm using spectral imagers consisting of two identical channels (CHA and CHB) that can simultaneously scan the northern and southern hemispheres (Cai et al., 2021; Eastes et al., 2020). GOLD observes Lyman-Birge-Hopfield (LBH) and OI 135.6 nm bands emissions during daytime but only the latter at night. OI 135.6 nm radiance is emitted as a result of recombination between oxygen ions and electrons (or negative ions) in the ionosphere. During the nighttime, the relationship between total radiance (in Rayleigh) for OI 135.6 nm emission and oxygen ion concentration indicate direct proportionality (England et al., 2008). Since the densities of oxygen ions and electrons are almost equal in the nighttime ionosphere, OI 136.5 nm emissions provide details about plasma (electron) density distribution in the magnetic meridional and zonal directions.

To investigate the diurnal variation of F layer true heights (hF) and evolution of ESF resulting from the development of EPBs for the days under study, ionospheric parameters observed by Digisondes at São Luís (Geogr: 2.3°S, 44°W; dip latitude: 2°S) and Fortaleza (Geogr: 3.9°S, 38.45°W; dip latitude: 9°S) stations, Brazil at 10 min cadence were collected and analyzed with the SAO Explorer software (Reinisch & Galkin, 2011). Figure 1 shows

the position of digisonde stations with respect to the solar terminator (ST) at 21:00 UT (~18:00 LT). During this time, Fortaleza and São Luís stations were on the nightside of ST, and their longitudes lie in the postsunset sector during which the eastward electric field in the F layer is enhanced. OI 136.5 nm nighttime emission scanned by GOLD can be used to observe the structure, number, and intensity of EPB but the onset time (~0–60 min after sunset) of these EPBs may not be ascertained from these emissions due to GOLD's routine east-west scanning that begins at about 20:10 UT and ends at about 00:10 UT during nighttime.

### 2.3. Model

To obtain storm-time perturbation in  $\mathbf{E} \times \mathbf{B}$  drift, simulations were carried out with the WACCM-X model. WACCM-X is one of NCAR's models that solves self-consistently the momentum, energy, and hydrostatic equations to model the coupled neutral atmosphere and ionosphere, low- and mid-latitude ionospheric dynamo using the same method as NCAR's Thermosphere-Ionosphere-Electrodynamics General Circulation Model (TIEGCM) described in detail by Qian et al. (2014). The version 2.2 used in this study has a horizontal resolution of  $0.9^\circ \times 1.25^\circ$  (latitude  $\times$  longitude) and extends from the Earth's surface to an altitude (pressure level) of  $4.1 \times 10^{-10}$  hPa corresponding to ~500–700 km depending on solar activity, and the atmosphere ranging from surface pressure to the stratosphere is constrained by reanalysis data from the Modern Era Retrospective Analysis for Research and Applications (MERRA; Rienecker et al. (2011)). Two different runs were made with each for storm- and quiet-time. The Weimer model which uses solar wind density, solar wind speed, north-south ( $B_z$ ), and west-east orientation of the Interplanetary Magnetic Field (IMF) (Weimer, 2005) and the Heelis model that uses Kp index (Heelis et al., 1982) were used to specify the energy input at high-latitude for storm-time and quiet-time runs respectively. The time step of the model output is 5 min.

## 3. Results

### 3.1. Geomagnetic Condition of 2–6 November 2021

Figure 2 shows the temporal variation of  $B_z$ ,  $E_y$ ,  $V_{sw}$ , SYM-H, and Kp indices between 02 and 06 November 2021 with each day demarcated by green vertical lines. The dark orange line represents the quiet day (November 13) geomagnetic indices for purpose of comparison. The arrival of CMEs released by the Sun on November 01 is reflected by a short-lived southward incursion of  $B_z$ , a very strong interplanetary shock wave and an abrupt change in the solar wind speed ( $V_{sw}$ ) from 450 to about 760 km/s at about 20:20 UT on November 03, causing a storm sudden commencement (SSC) and launched the initial phase (IP) of the storm.

A second short-living  $B_z$  southward incursion at about 00:30 UT on November 04 and a subsequent large southward incursion caused the storm's main phase (MP). The east-west component of the electric field ( $E_y$ ) turned eastward at about 20:00 UT and reached values of ~12.8 and 14.94 mV/m at 21:19 and 09:00 UT of November 03 and 04 respectively, almost in consonance with the minimum  $B_z$  values. The beginning of MP is characterized by a northward orientation of  $B_z$  (as seen at about 00:00 UT on November 4) and the recovery of the magnetospheric shielding electric field that can subsequently lead to an overshielding electric field (PEF) (Abdu, 2012; Santos et al., 2012). The symmetric component of the ring current (SYM-H) indicates the disturbance in the geomagnetic main field in equatorial regions and its dip in value is a pointer to the severity of a geomagnetic disturbance, possible penetration of the electric field into the low-latitude ionosphere, and/or change of storm phase. At SSC, the SYM-H abruptly deviated from 0 to about ~50 nT and then dipped to about –20 nT during the IP stage. During the MP stage, SYMH dipped to ~–105 nT and then to about –118 nT prior to a reversal indicating the start of the recovery phase (RP).

At about 13:00 UT, it can be noted that  $B_z$  turned northward and other indices changed orientation in consonance, during RP. According to Abdu (2012) and references contained therein, three forcings that can influence equatorial electrodynamics during this phase, are: (a) Disturbance dynamo wind from high latitudes oriented westward as a result of Coriolis forces, (b) The westward oriented DDEF, and (c) PEF associated with the northward orientation of  $B_z$  as seen for instance, during the beginning of the recovery phase of the storm. The effect of DDEF can last for up to few days during which its polarity can change as seen in the fluctuation of F layer height (see e.g., Blanc and Richmond (1980); Abdu (2012) and references therein). November 2, 5, and 6 also exhibit features of weak to moderate geomagnetic disturbances as seen from the persistent fluctuation in  $B_z$  and  $E_y$  on November 2 and three fast southward incursions of  $B_z$  at 05:05, 13:00, and 14:30 UT on November 5. The SYMH

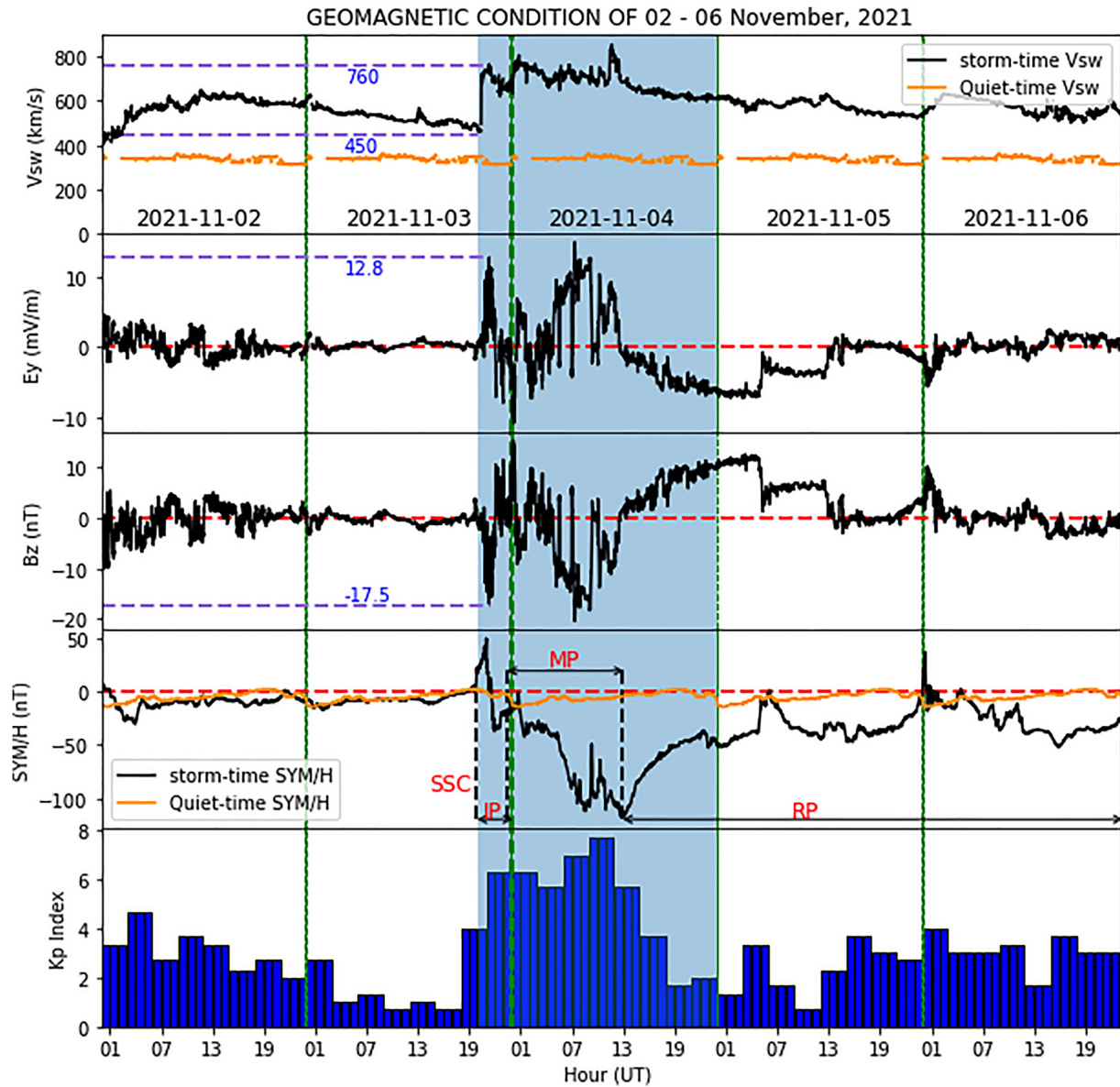


**Figure 2.** From top to bottom, Solar wind speed ( $V_{sw}$ ), East-West component of the Interplanetary electric field ( $E_y$ ), North-South Component of Interplanetary Magnetic Field ( $B_z$ ), Symmetric-H (SYM-H) that is equivalent to the Dst index and Kp index between 02–06 November 2021. All parameters have a 1-min resolution except the Kp index which is 3-hourly. The blue shaded regions show the period of high geomagnetic activity extending from sunset on November 3.

of November 5 and 6 exhibit similar features, with their values dipping to  $\sim -50$  nT at about 15:30 and 16:30 UT respectively, signifying moderate storm events.

### 3.2. On the Intensity of EPBs and ESF

Figure 3 shows scans obtained from the northern and southern hemispheres by GOLD at 15-min intervals between 23:10 and 23:40 UT from 2 to 5 and 13 November 2021. The red line indicates the magnetic equator while the regions of intense brightness due to high plasma densities on the northern and southern sides of the magnetic equator are northern and southern EIA crests respectively. The dark stripes cutting across the magnetic equator in the magnetic meridian direction and extending poleward are regions of reduced photon emissions due to depletion in plasma density known as EPBs. These EPBs drift from west to east at a speed ranging from  $\sim 20$  to 190 m/s (de Paula et al., 2002; Karan et al., 2020) as GOLD scans from east to west. This implies that EPBs shift eastward for successive GOLD scans and subsequently out of GOLD's view.

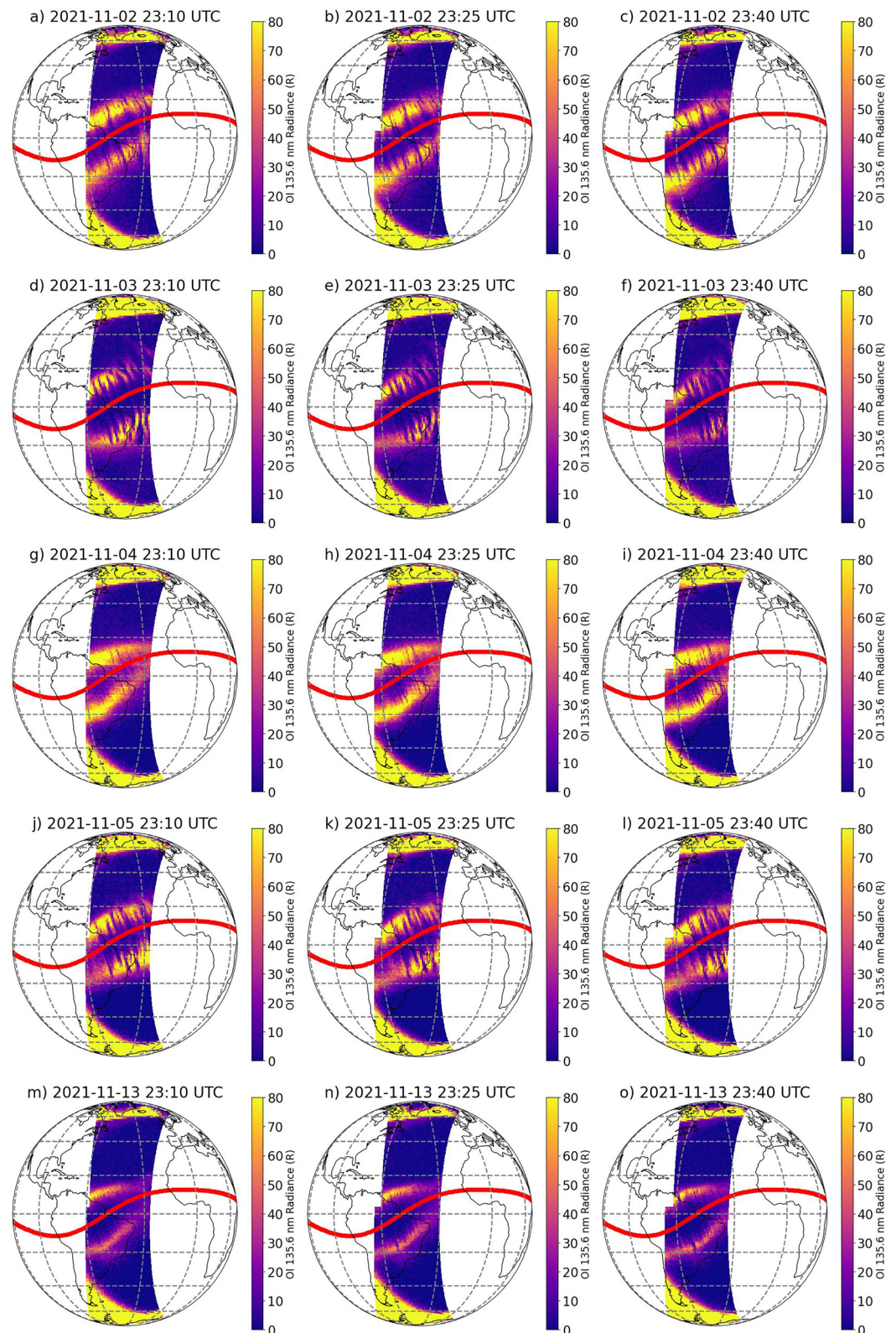


**Figure 3.** OI 135.6 nm radiance imaged by GOLD between 23:10 and 23:40 UT for November 3 – 5 and 13 November 2021, showing regions of enhanced plasma density on either side of the geomagnetic equator (red line) known as equatorial ionization anomaly (EIA) crests (yellow regions between  $\pm 20^\circ$ ) and regions of depleted (low density) plasma known as equatorial plasma bubbles (EPBs). EPB development was intensified on November 3 but weakened on November 4. November 13 is a quiet day.

**Table 1**  
Summary of EPB Characteristics Between 2–5 and 13 November 2021

Day	No. of EPBs	ME (Geogr)	PE (N)	PE (S)	ML (N)	ML (S)	$\Delta$ ML
November 2	4	3.2	17.1	−15.3	13.9	18.1	4.2
November 3	6	7.8	23.8	−19.2	16	27.0	11.0
November 4	2	5.3	13.4	−5.9	8.1	11.2	2.9
November 5	5	1.2	12.2	−18.1	11	19.3	8.3
November 13	2	−4.4	4.2	−17.3	8.6	13	4.4

Note. PE is the poleward edge of the most extended EPB in the Northern (N) and Southern (S) hemispheres, ME is the geographic latitude of a point on the magnetic equator perpendicular to the EPB axis from which PE is measured, ML is the latitudinal extension of EPBs in magnetic meridian direction, and  $\Delta$ ML is the difference between ML in the Northern and Southern hemispheres. All parameters from column 3 to 8 are in degrees (°) and measured at 23:25 UT.

The intensity of EPBs will be described in terms of their meridional extension with respect to the magnetic equator and EIA crests. For instance, Cherniak and Zakharenkova (2016) described EPBs that extended to mid-latitudes due to storm-time disturbance fields as super EPBs. Table 1 shows the meridional extension of the EPBs in Figure 3. PE is the poleward edge of the most extended EPB in the Northern (N) and Southern (S) hemispheres as indicated by the white dots on Figure 3, ME is the geographic latitude of a point on the magnetic equator perpendicular to the EPB axis from which PE is measured, ML is the latitudinal extension of EPBs in the magnetic meridian direction in each hemisphere (N and S), and  $\Delta$ ML is the difference between ML in the Northern and Southern hemispheres. All parameters are in degrees (°) and measured at 23:25 UT except the Number of EPBs (counted at 23:10 UT).

From Table 1, it can be seen that the most extended EPBs on Nov. 2, 3, 4, 5, and 13 in the northern hemisphere extend from the magnetic equator by approximately 14, 16, 8, 11, and 8°, and by 18, 27, 11, 19, and 13° in the southern hemisphere respectively. Thus, the latitudinal extension is least on November 4 (smaller than November 13 which is a quiet day) and highest

on November 3. It can also be seen that the extension correlates with geomagnetic activity except for a deviation on November 4. Considering ML, EPB development on November 3 can be said to be intensified but weak on November 4.

Furthermore, the asymmetry in EPB latitudinal extension indicated by  $\Delta$ ML follows a similar trend as ML. EPBs extend further in the Southern hemisphere than the Northern hemisphere for all days under study, implying that the observed asymmetry may be due to the background neutral wind since it was present on all days. This asymmetry was highest on November 3 with a value of  $\sim 11^\circ$  and least on November 4 (again, lower than that of November 13 which is a quiet day).

Additionally, there are more, and closely clustered EPBs on November 3 as compared to November 4 with a lower number of EPBs and a sparser distribution. Also, the EPBs on November 3 seem to drift eastward with no new EPBs evolving as compared to other days at 23:40 UT. This suggests that the EPBs of November 3 may have been formed as a result of the eastward-oriented PPEF at about 21:00 UT (see Figure 2) that caused a strong upwelling from which EPBs developed as discussed by Tsunoda (2015), while a possible change in polarity due to PEF may have impeded the development of new EPBs as seen at 23:40 UT during which the EIA crests can be seen to be converging toward the magnetic equator.

Figure 4 shows ionograms for November 2 – 5 and 13, 2021, showing the reflection of radio waves by the F-layer plasma over SL (2.3°S, 44°W, 2°S dip latitude). The third column shows the scattering of these radio waves by plasma irregularities. These scatterings are well known as ESF and are manifestations of EPBs. The first column shows the ionospheric reflections 10 min before sunset with well-defined critical frequencies while the second column shows reflections 10 min after sunset. Observe that the F layer at 20:40 UT was lowest on November 4 and 13 (quiet day) and as such, the weakening force did not appear abruptly at sunset but seems to be present prior to sunset. It is important to note that September to March are months of high EPB occurrence and as such, EPB/ESF development is expected on each night of these months for the Brazilian longitudinal sector (Abdu et al., 2003). This also confirms that the weakening of EPB on November 4 is due to a geomagnetic disturbance despite the time difference between SSC and sunset on this day. Also observe the early onset of ESF on November 3, about 30 min after the abrupt southward excursion of Bz that initiates the storm as shown in Figure 2. This early onset is a clear deviation from other days and also suggests the influence of a geomagnetic disturbance that occurred on that day. The third column shows the types of ESF at 22:00 UT (19:00 LT) with mixed spread F (MSF) observed on November 2, range spread F (RSF) occurring on November 4 and 13 (Figures 4i and 4o) while strong range spread F (SSF) occurred on November 3 and 5 (Figures 4f and 4l). It can be seen that ESF activity was weak on November 4 and 13 but intense on November 3 and 5. The altitudinal extension of the spread peaked on November 3 compared to other days under study, thus, giving rise to the strongest ESF.

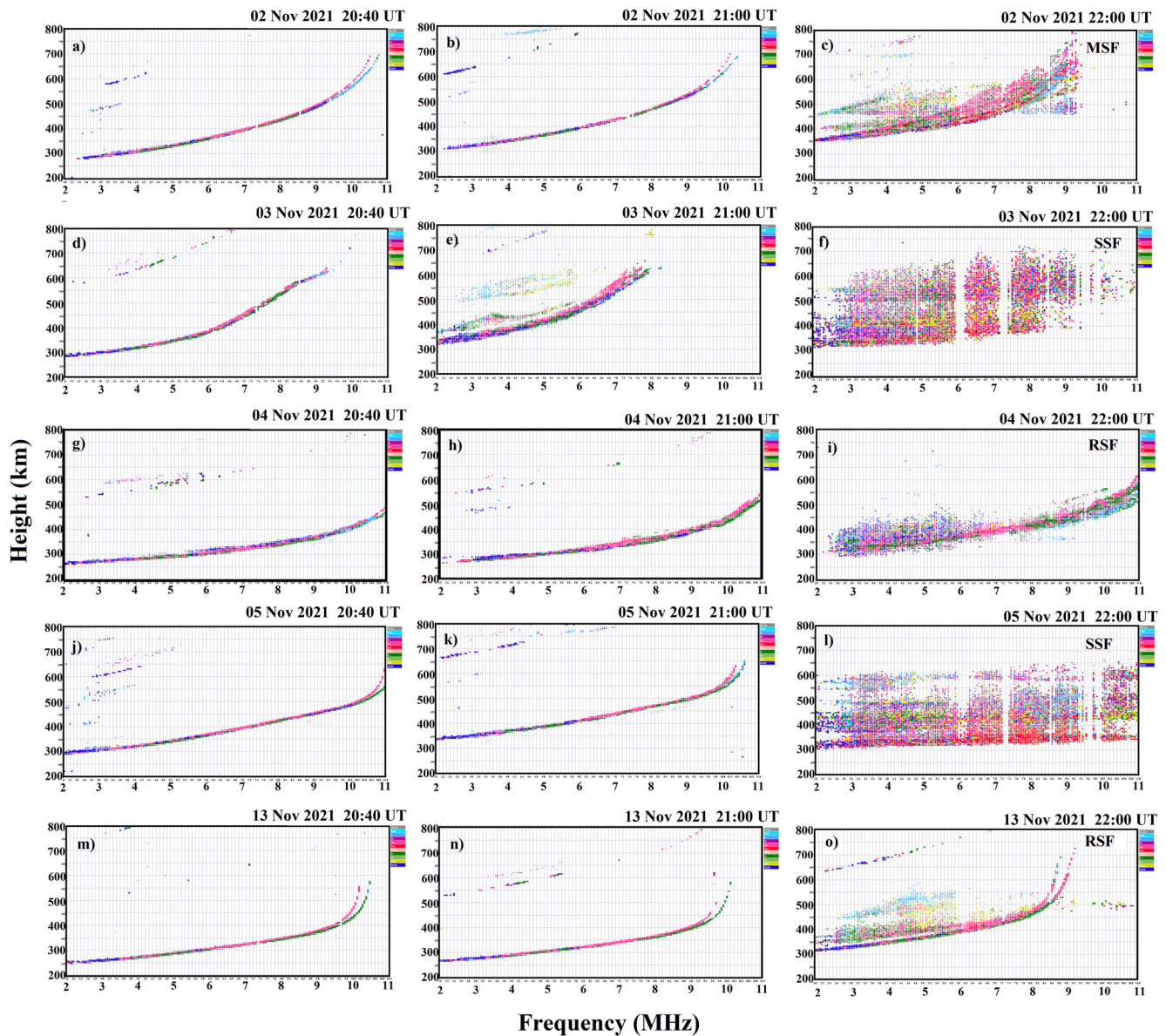


**Figure 4.** Ionograms showing reflections and scattering of radio waves by the F layer height at 20:40, 21:00, and 22:00 UT corresponding to pre-sunset, sunset, and postsunset epochs. The strongest spread of frequencies was observed on November 3 during which the earliest onset was also observed as seen at 21:00 UT, while the weakest frequency spreads were observed on November 4 and 13.

### 3.3. Evidence of Disturbance Electric Fields

Figure 5 shows the variation in the F region's true height ( $hF$ ) over São Luís Digisonde station from 2 to 5 (Figures 4a–4d) and 12 to 13 (Figures 4e and 4f), November 2021 at plasma frequencies ranging from 3 to 7 MHz. Figures 4e and 4f represent two quiet days in the month of November 2021. The local time (LT) at this station is UT–3h and the blue shaded regions indicate the period of postsunset rise (PSSR) or PRE in the F region prior to a downward drift. For purpose of discussion, only the  $hF$  at which the 7 MHz frequency is reflected will be considered and will be referred to as  $hF_7$  where necessary. During PSSR,  $hF_7$  reached ~440 km on November 2, at least 450 km on November 3, ~350 km on November 4, and ~420 km on November 5. The peak reached by  $hF_7$  on November 3 may have exceeded 450 km if not for a data gap at 21:00 UT (18:00LT). The quiet time  $hF$  of November 12 and 13 at PRE reached ~420 and 370 km respectively. It can be seen that  $hF_7$  at PRE on November 3 exceeds other observed days by ~50–100 km while that of November 4 is less than all observed days, including quiet days by ~20–100 km.

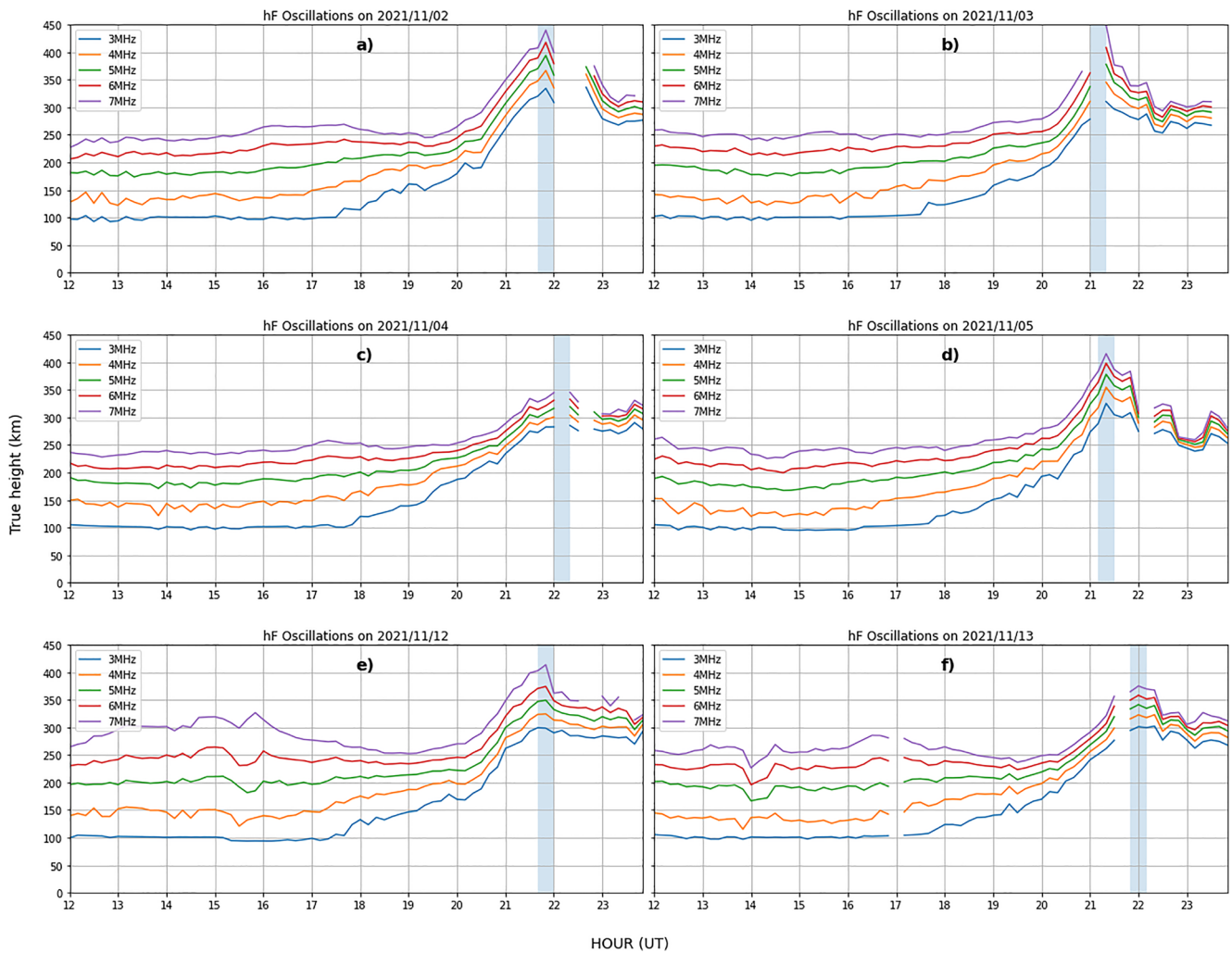


**Figure 5.** Day-to-day variation in F layer height measured by ionosondes at the São Luís (SL) station. The increase in F layer height at sunset is known as PRE. The magnitude of PRE is highest on November 3 ( $\geq 450$  km) and least on November 4 compared to other days studied here.

The increase in F layer height on November 3 is similar to the change in height observed by Santos et al. (2012) in their Figure 3 that corresponds to a PRE of  $\sim 50$  m/s and a zonal electric field of  $\sim 1.5$  mV/m oriented eastward and was possibly associated with a penetration electric field. The F layer over Fortaleza drifted vertically upwards with a speed of  $\sim 34$ ,  $\sim 48$ ,  $\sim 21$ , and  $\sim 30$  m/s (not shown here) at PRE time with the peak hF7 reached at 21:50, 21:10, 22:10, and 21:20 UT on November 2, 3, 4, and 5 respectively, resulting in an average drift value of  $\sim 38$  m/s which is less than the PRE of November 3 by  $\sim 10$  m/s and greater than that of November 4 by  $\sim 17$  m/s. Thus, the PRE at São Luís with closer proximity to the magnetic equator may exceed 50 m/s on November 3, assuming there is a contribution from the evening time E region in both hemispheres, as proposed by Farley et al. (1986). During the initial phase of a storm, an eastward-oriented electric field can penetrate into the low-latitude ionosphere and influence in-situ electrodynamics, and Fejer et al. (2008) observed that eastward-oriented penetrating fields at about sunset enhance vertical drift by about 5–15 m/s. It can be seen that the PRE observed on November 3 occurred at about SSC and follows the abrupt increase in the solar wind speed from 450 to  $\sim 760$  km/s and a southward turning of  $B_z$  as shown in Figure 2. Since the shielding effect of the region 2 field-aligned currents can be ineffective within this time scale ( $\sim 30$  min) as indicated by C.-S. Huang et al. (2007), it implies that there may have been a high penetration efficiency during this time, thereby raising the F region to a higher altitude.

The decrease in height on November 4 occurred during the storm's recovery phase. DDEF due to disturbance wind, typical of this phase and usually oriented westward, can be present during this time. Fejer et al. (2008) observed that this westward-oriented disturbance electric field results in downward (negative) vertical drift

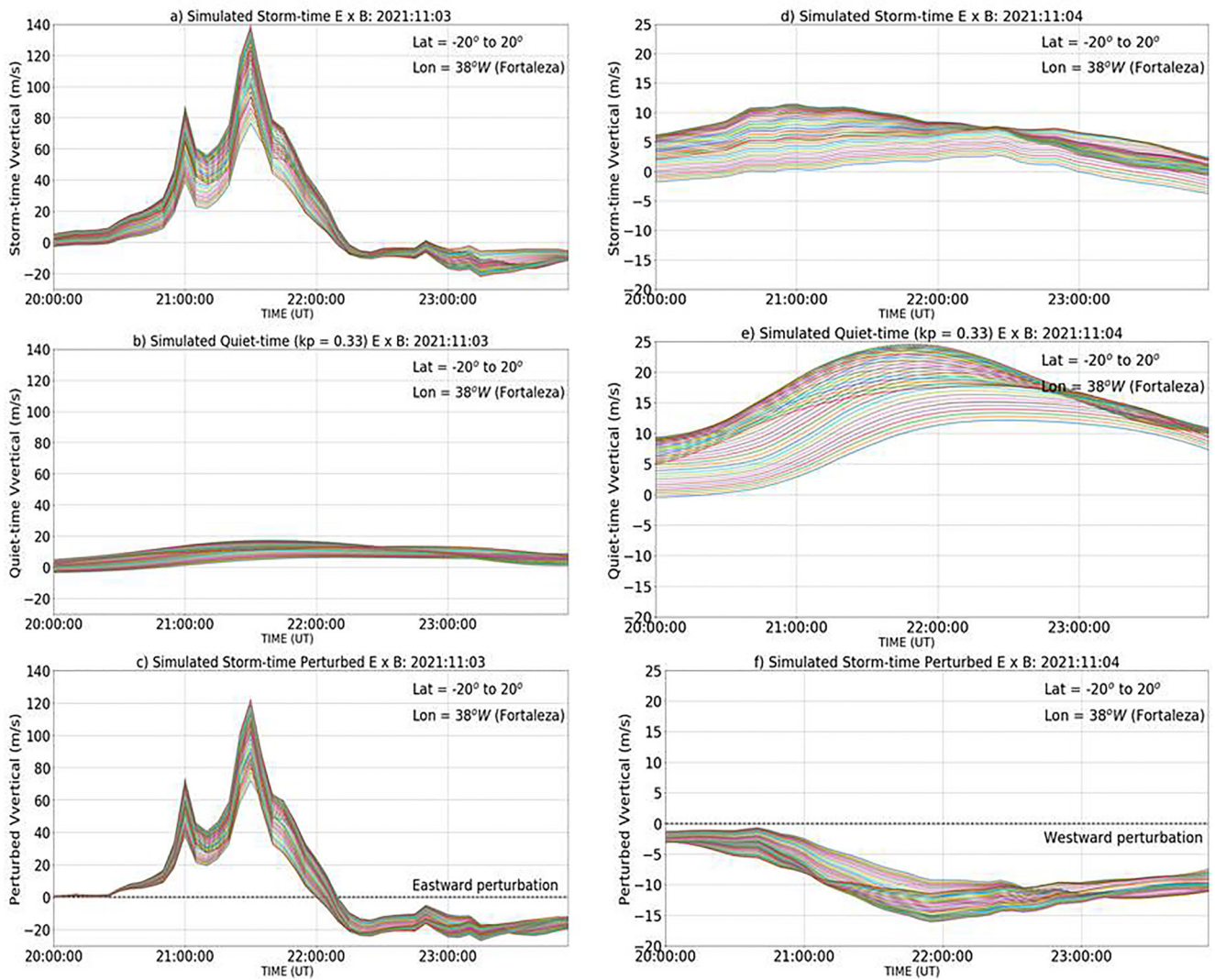


**Figure 6.** Simulated vertical  $\mathbf{E} \times \mathbf{B}$  drift for November 3 and 4 2021. a and b are the storm-time  $\mathbf{E} \times \mathbf{B}$  drift, c, and d are the quiet-time  $\mathbf{E} \times \mathbf{B}$  drift while e and f are the storm-perturbed  $\mathbf{E} \times \mathbf{B}$  drift oriented upward (eastward E) and downward (westward E) on November 3 and 4 respectively. The colored lines indicate the  $\mathbf{E} \times \mathbf{B}$  drift from  $\pm 20^\circ$  latitude.

perturbation. The superimposition of this downward drift on the background drift (due to neutral wind dynamo) results in a decrease of the effective vertical drift and thus, the observed lower-than-quiet time F layer height on November 4. Abdu (2012) observed a similar lower-than-quiet time F layer height and suggested that it was associated with a westward over-shielding electric field (PEF). Furthermore, the storm of 10 November 2004, also observed by Abdu (2012) had its initial phase on November 9 and orchestrated F layer height suppression about 20 hr later due to DDEF oriented westward at sunset. Thus, sunset on November 4 is still within the range of influence of westward disturbance fields.

F layer height can be influenced by the background neutral wind, E region conductivity, upward propagating waves or large-scale wave structures, and disturbance electric fields. Quantifying the contribution of each of the aforementioned influences is difficult, hence the need for simulations. Figure 6 shows simulated vertical  $\mathbf{E} \times \mathbf{B}$  drift from WACCM-X for November 3 and 4. Note that the y-axis for November 3 and 4 is scaled from  $-20$  to  $140$  and  $-20$  to  $25$  respectively so as to ensure visual clarity. Figures 5a and 5d are the storm-time vertical drift and Figures 5b and 5e are the quiet-time vertical  $\mathbf{E} \times \mathbf{B}$  drift. Figures 5c and 5f are the perturbations obtained from the difference of storm- and quiet-time vertical  $\mathbf{E} \times \mathbf{B}$  that result in upward (positive) and downward (negative) perturbations respectively. The storm-time  $\mathbf{E}$  reached values of  $2.5$  and  $3.2$  mV/m at  $21:00$  and  $21:30$  UT respectively on November 3 and about  $0.003$  mV/m at  $21:30$  UT on November 4, and as expected, resulted in the enhanced and weakened peak vertical

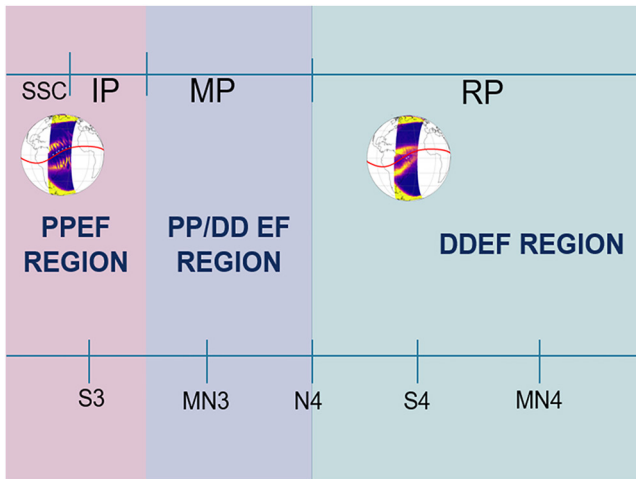


**Figure 7.** Initial phase (IP) coincides with sunset (S3) on November 3 while recovery phase (RP) coincides with sunset (S4) on November 4. IP is in the prompt penetration electric field (PPEF) region (eastward  $\mathbf{E}$ ) and thus increases the magnitude of Pre-reversal Enhancement (PRE), while RP is in the disturbance dynamo electric field (DDEF) region (westward  $\mathbf{E}$ ) and as such, annuls eastward  $\mathbf{E}$  and consequently weakens PRE. MN and N imply morning and Noon respectively.

drift of November 3 and 4 respectively. These perturbations are similar to those observed by Fejer et al. (2008) in which PPEF (DDEF) produced perturbations in the postsunset drift oriented upward (downward). In addition to day-to-day variations in F layer heights over SL observed by digisondes, the simulation provides numerical evidence of the presence of eastward-oriented PPEF and westward-oriented DDEF at sunset on November 3 and 4 respectively.

## 4. Discussion

### 4.1. On the Onset and Evolution of EPBs/ESF

The extension of EPBs on November 3, 4, and 5 in the southern hemisphere reached dip latitudes of  $\sim 19$ ,  $\sim 6$ , and  $\sim 18^\circ$  respectively. These latitudes correspond to flux-tube apex height of  $\sim 915$ ,  $\sim 250$ , and  $\sim 550$  km, representing altitudes reached by plasma on these days, prior to a poleward drift along magnetic field lines. Additionally, these altitudes correspond with the magnitude of plasma height observed by digisondes as shown in Figure 5. Since PRE occurred at about 21:10 UT on November 3, which is 10–60 min earlier than preceding and succeeding days under study, it indicates that eastward  $\mathbf{E}$  was present for a longer duration on November 3, allowing plasma to drift to higher latitudes assuming that the time of change of electric field polarity is the same for the days under study. Since an increase in the duration of eastward  $\mathbf{E}$ , especially under storm conditions, can enhance the magnitude of  $\mathbf{E} \times \mathbf{B}$  drift (C.-S. Huang et al., 2005), the long duration of eastward  $\mathbf{E}$  on November 3 appears to cause plasma to drift to a high flux tube height and subsequently drift to a higher latitudinal extension as seen in the magnitude of ML and  $\Delta ML$ .

In addition to the duration of eastward electric field, its magnitude due to superimposition of storm and background contributions influenced the intensity of EPBs during the initial phase of the storm on November 3 as illustrated in Figure 7. S3 (pink background) and S4 (green background) cover sunset on November 3 and 4 respectively while MN3 and MN4 are their corresponding midnight. During the IP of the storm on November 3, eastward-oriented PPEF was present as evidenced in the abrupt increase in  $E_y$  (see Figure 2) that started at about 20:10 UT and the increase in the peak F layer height shown in Figure 5b. The coincidence between PPEF during the IP, and S3 during which the F region neutral wind dynamo drives the eastward oriented  $\mathbf{E}$ , results in an enhanced eastward zonal  $\mathbf{E}$  whose interplay with the horizontally oriented  $\mathbf{B}$  at the dip equator results in an enhanced upward vertical  $\mathbf{E} \times \mathbf{B}$  drift, which drives large RTI growth as well as rapid lift of the F layer to higher flux-tube apex height. This initiates the development of field-aligned topside irregularities initiated by RTI along unstable flux tubes at higher altitudes, and results in EPB and ESF intensification observed by GOLD and ionosondes on November 3. Thus confirming the strong-vertical-drift-EPB-early-onset relationship hypothesized by Martinis et al. (2021).

During the RP, the disturbance dynamo winds that characterize this phase of a storm drive DDEF that are typically oriented westward at sunset. DDEF can have a lifetime ranging from about 2 hr after PPEF to up to 30 hr after the start of a storm (Abdu (1997, 2012), and references therein). The green background in Figure 7 is the DDEF region and coincides with S4. The westward orientation of DDEF is evidenced in suppression of the peak F layer height to lower-than-quiet-time as shown in Figure 5c and the simulated storm driven downward  $\mathbf{E} \times \mathbf{B}$  shown in Figure 6f. This results in stability of the F layer that delays ESF (EPB) onset and weakens EPB development. GOLD also shows an increase in plasma density as indicated in the intensity of emitted photons that exceeded 100R on November 4 compared to quiet time (November 13). Since ion-neutral collision frequency can be high at low altitudes and undermine the contribution of the gravity term ( $\frac{g}{\nu}$ ; where  $g$  is the acceleration due to gravity and  $\nu$  is the ion-neutral collision frequency) to the total RTI growth rate (Kelley, 2009; Sultan, 1996), this may have also contributed to the weakening of EPB development on November 4.

### 4.2. On the Meridional Extension of EPBs

Table 1 shows a positive relationship between the meridional extension of EPBs and geomagnetic activity, with the most (least) extended EPBs observed on November 3 (4). A point of interest in this study is the hemispheric

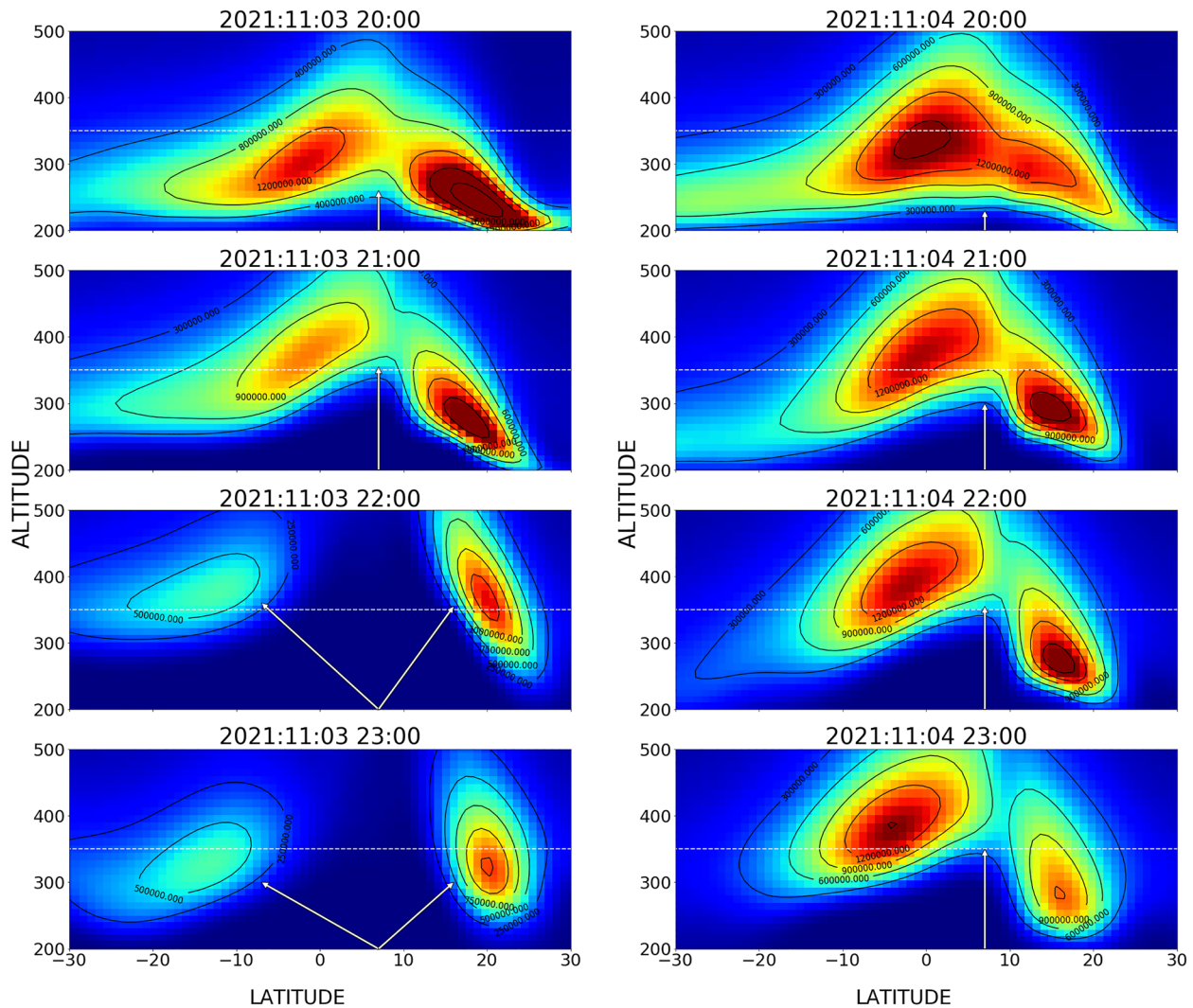


**Figure 8.** Simulated plasma distribution on the adjacent sides of the magnetic equator at the Fortaleza longitudes. Plasma height is greater in the southern hemisphere on both November 3 and 4. The overall plasma height is greater on November 3 than 4 due to vertical  $\mathbf{E} \times \mathbf{B}$  drift.

asymmetry in ML ( $\Delta ML$ ) observed for all days under study including quiet days. This day-to-day presence of  $\Delta ML$  suggests that the geomagnetic disturbance is not responsible for observed asymmetry. However, the magnitude of  $\Delta ML$  seems to be influenced by the magnitude of  $\mathbf{E} \times \mathbf{B}$  drift since it increases with an increase in F layer height.

Figure 8 illustrates the asymmetry in the distribution of plasma in the northern and southern hemispheres for November 3 and 4 at  $\sim 34^\circ W$  as simulated by WACCM-X. It is evident that (a) Plasma in the southern hemisphere is lifted to higher altitudes as compared to the northern hemisphere for both days, indicating an altitudinal asymmetry in plasma distribution between the two hemispheres, and (b) The meridional extension of the EIA crest is greater in the southern hemisphere, where the F-layer is lifted to higher altitude. Therefore the increase in the latitudinal extension in the southern hemisphere is due to the presence of north-south asymmetry in plasma altitude. Consistent with the findings of Cai et al. (2022), the north-south asymmetry ( $\Delta ML$ ) is likely associated with the prevailing northward meridional winds in November, which transport plasma to higher altitudes in the southern hemisphere but to lower altitudes in the northern hemisphere. On the other hand, as discussed earlier, the more polarward extension of the EIA crest on November 3 is associated with the enhancement in the eastward  $\mathbf{E}$  associated with storm-time PPEF, which lifts plasma to higher altitudes and further away from the magnetic equator, thus, the geomagnetic disturbance electric fields influenced the magnitude of the hemispheric asymmetry.

## 5. Conclusion

Numerous studies mentioned in the first section have observed storm-time effects on the evolution of equatorial irregularities, especially EPBs, and ESF under weak, moderate, and strong storm conditions. The peculiarity of each storm has made the accurate prediction of storm-time EPB/ESF evolution difficult. However, it is now known that disturbance electric fields and their orientation, disturbance wind, ion-neutral interactions, and local time of storm event at a particular longitude are essential factors that orchestrate the enhancement, weakening, or suppression of EPBs. In this study, we have presented intensification (weakening) of EPB development on November 3 (4), which is manifested in the high (low) flux tube height reached by plasma and the large (small) latitudinal extension of EPBs, using multi-instrument observations and simulation. Both approaches attest that the geomagnetic conditions of November 3 and 4 influenced the electrodynamics of the equatorial ionosphere and subsequent development of EPBs. The main findings of this study include:

1. There was an intensification (weakening) of EPB development on November 3 (4). Evidence of this intensification (weakening) can be seen in the latitudinal extension of EPBs and the asymmetry in latitudinal extension between the southern and northern hemispheres.
2. The intensification (weakening) of EPB development is due to the interference between eastward (westward) oriented PPEF at the storm IP (DDEF at the storm RP) during PRE. This lifts (pulls down) the F layer and provided favorable (unfavorable) conditions for RTI growth (weakening) and consequent EPB enhancement (weakening).
3. The asymmetry in latitudinal extension between the northern and southern EIA crests is enhanced on November 3 compared to November 4, indication that asymmetry can be influenced by geomagnetic activity.

## Data Availability Statement

GOLD data is available at <https://gold.cs.ucf.edu/>. The ionosonde data can be accessed via <https://embracedata.inpe.br/ionosonde> and processed with the SAO explorer software available via <https://ulcar.uml.edu/SAO-X/SAO-X.html>. The WACCM-x electron density and drift data for 3 and 4 November 2021, as well as python codes can be obtained via <https://doi.org/10.5281/zenodo.7865397> (Amadi, 2023).

## References

- Abdu, M. (1997). Major phenomena of the equatorial ionosphere-thermosphere system under disturbed conditions. *Journal of Atmospheric and Solar-Terrestrial Physics*, 59(13), 1505–1519. [https://doi.org/10.1016/s1364-6826\(96\)00152-6](https://doi.org/10.1016/s1364-6826(96)00152-6)
- Abdu, M. (2001). Outstanding problems in the equatorial ionosphere-thermosphere electrodynamics relevant to spread f. *Journal of Atmospheric and Solar-Terrestrial Physics*, 63(9), 869–884. [https://doi.org/10.1016/s1364-6826\(00\)00201-7](https://doi.org/10.1016/s1364-6826(00)00201-7)
- Abdu, M. (2012). Equatorial spread f/plasma bubble irregularities under storm time disturbance electric fields. *Journal of Atmospheric and Solar-Terrestrial Physics*, 75, 44–56. <https://doi.org/10.1016/j.jastp.2011.04.024>
- Abdu, M., Batista, I., Takahashi, H., MacDougall, J., Sobral, J., Medeiros, A., & Trivedi, N. (2003). Magnetospheric disturbance induced equatorial plasma bubble development and dynamics: A case study in Brazilian sector. *Journal of Geophysical Research*, 108(A12), 1449. <https://doi.org/10.1029/2002ja009721>
- Alam Kherani, E., De Paula, E. R., & Berton, F. C. (2004). Effects of the fringe field of Rayleigh-Taylor instability in the equatorial E and valley regions. *Journal of Geophysical Research*, 109(A12), A12310. <https://doi.org/10.1029/2003ja010364>
- Amadi, B. C. (2023). WACCMX storm quiet time EDENS and EXB [Dataset]. Zenodo. <https://doi.org/10.5281/zenodo.7865397>
- Bhattacharyya, A. (2022). Equatorial plasma bubbles: A review. *Atmosphere*, 13(10), 1637. <https://doi.org/10.3390/atmos13101637>
- Bhattacharyya, A., Fedrizzi, M., Fuller-Rowell, T., Gurrum, P., Kakad, B., Sripathi, S., & Sunda, S. (2019). Effect of magnetic storm related thermospheric changes on the evolution of equatorial plasma bubbles. *Journal of Geophysical Research: Space Physics*, 124(3), 2256–2270. <https://doi.org/10.1029/2018ja025995>
- Blanc, M., & Richmond, A. (1980). The ionospheric disturbance dynamo. *Journal of Geophysical Research*, 85(A4), 1669–1686. <https://doi.org/10.1029/ja085ia04p01669>
- Cai, X., Burns, A. G., Wang, W., Qian, L., Liu, J., Solomon, S. C., et al. (2021). Observation of postsunset oi 135.6 nm radiance enhancement over South America by the gold mission. *Journal of Geophysical Research: Space Physics*, 126(2), e2020JA028108. <https://doi.org/10.1029/2020ja028108>
- Cai, X., Qian, L., Wang, W., McInerney, J. M., Liu, H.-L., & Eastes, R. W. (2022). Hemispherically asymmetric evolution of nighttime ionospheric equatorial ionization anomaly in the American longitude sector. *Journal of Geophysical Research: Space Physics*, 127(11), e2022JA030706. <https://doi.org/10.1029/2022ja030706>
- Carter, B., Retterer, J., Yizengaw, E., Groves, K., Caton, R., McNamara, L., et al. (2014). Geomagnetic control of equatorial plasma bubble activity modeled by the TIEGCM with KP. *Geophysical Research Letters*, 41(15), 5331–5339. <https://doi.org/10.1002/2014gl060953>
- Carter, B., Yizengaw, E., Pradipta, R., Retterer, J., Groves, K., Valladares, C., et al. (2016). Global equatorial plasma bubble occurrence during the 2015 St. Patrick's Day storm. *Journal of Geophysical Research: Space Physics*, 121(1), 894–905. <https://doi.org/10.1002/2015ja022194>
- Chang, H., Kil, H., Sun, A. K., Zhang, S.-R., & Lee, J. (2022). Ionospheric disturbances in low-and midlatitudes during the geomagnetic storm on 26 august 2018. *Journal of Geophysical Research: Space Physics*, 127(2), e2021JA029879. <https://doi.org/10.1029/2021ja029879>

### Acknowledgments

B.C. Amadi expresses his sincere appreciation to NCAR's Advanced Student Program's Graduate Visiting Program (ASP-GVP) sponsored by the National Science Foundation, for a visiting Fellowship, Coordenacao Aperfeiçoamento de Pessoal de Nivel Superior (CAPES) and to Conselho Nacional de Desenvolvimento Cientifico e Tecnológico (CNPQ) for student support under the process numbers 00.889.834/000-108 and 164435/2021-2 respectively. L. Qian is supported by NASA Grants 80NSSC19K0278, 80NSSC20K1350, 80NSSC20K0721, and 80NSSC20K0189. E.R. de Paula thanks the INCT GNSS-NavAer Project under Grants CNPq 465648/2014-2 and FAPESP 2017/50115-0, the Brazilian Ministry of Science, Technology, and Innovation, the Brazilian Space Agency and the CNPq 202531/2019-0 project. A. M. Santos would like to thank the China-Brazil Joint Laboratory for Space Weather (CBJLSW), National Space Science Center (NSSC), Chinese Academy of Sciences (CAS) for supporting her postdoctoral research. S. A. Sanchez thanks CAPES and FAPESP under process numbers 88887.351785/201-900 and 2023/0780-79 respectively. The authors also thank the GOLD instrument team at LASP, University of Colorado. The authors are also grateful to Richard W. Eastes and another reviewer for helpful suggestions and patiently reviewing this article.

- Cherniak, I., & Zakharenkova, I. (2016). First observations of super plasma bubbles in Europe. *Geophysical Research Letters*, 43(21), 11–137. <https://doi.org/10.1002/2016gl071421>
- Cherniak, I., Zakharenkova, I., & Sokolovsky, S. (2019). Multi-instrumental observation of storm-induced ionospheric plasma bubbles at equatorial and middle latitudes. *Journal of Geophysical Research: Space Physics*, 124(3), 1491–1508. <https://doi.org/10.1029/2018ja026309>
- de Paula, E. R., de Oliveira, C., Caton, R. G., Negreti, P. M., Batista, I. S., Martinon, A. R., et al. (2019). Ionospheric irregularity behavior during the September 6–10, 2017 magnetic storm over Brazilian equatorial–low latitudes. *Earth Planets and Space*, 71(1), 1–15.
- de Paula, E. R., Kantor, I., Sobral, J., Takahashi, H., Santana, D., Gobbi, D., et al. (2002). Ionospheric irregularity zonal velocities over cachoeira paulista. *Journal of Atmospheric and Solar-Terrestrial Physics*, 64(12–14), 1511–1516. [https://doi.org/10.1016/s1364-6826\(02\)00088-3](https://doi.org/10.1016/s1364-6826(02)00088-3)
- Eastes, R., McClintock, W., Burns, A., Anderson, D., Andersson, L., Aryal, S., et al. (2020). Initial observations by the gold mission. *Journal of Geophysical Research: Space Physics*, 125(7), e2020JA027823. <https://doi.org/10.1029/2020ja027823>
- Eastes, R., McClintock, W., Burns, A., Anderson, D., Andersson, L., Codrescu, M., et al. (2017). The global-scale observations of the limb and disk (GOLD) mission. *Space Science Reviews*, 212(1), 383–408. <https://doi.org/10.1007/s11214-017-0392-2>
- Eccles, J., St. Maurice, J., & Schunk, R. (2015). Mechanisms underlying the prereversal enhancement of the vertical plasma drift in the low-latitude ionosphere. *Journal of Geophysical Research: Space Physics*, 120(6), 4950–4970. <https://doi.org/10.1002/2014ja020664>
- Eccles, J. V. (1998). Modeling investigation of the evening prereversal enhancement of the zonal electric field in the equatorial ionosphere. *Journal of Geophysical Research*, 103(A11), 26709–26719. <https://doi.org/10.1029/98ja02656>
- England, S., Immel, T., & Huba, J. (2008). Modeling the longitudinal variation in the post-sunset far-ultraviolet oi airglow using the SAMI2 model. *Journal of Geophysical Research*, 113(A1), A01309. <https://doi.org/10.1029/2007ja012536>
- Farley, D., Bonelli, E., Fejer, B. G., & Larsen, M. (1986). The prereversal enhancement of the zonal electric field in the equatorial ionosphere. *Journal of Geophysical Research*, 91(A12), 13723–13728. <https://doi.org/10.1029/ja091ia12p13723>
- Fejer, B. G., Immel, T., & Su, S.-Y. (2008). Seasonal and longitudinal dependence of equatorial disturbance vertical plasma drifts. *Geophysical Research Letters*, 35(20), L20106. <https://doi.org/10.1029/2008gl035584>
- Fesen, C., Crowley, G., Roble, R., Richmond, A., & Fejer, B. (2000). Simulation of the pre-reversal enhancement in the low latitude vertical ion drifts. *Geophysical Research Letters*, 27(13), 1851–1854. <https://doi.org/10.1029/2000gl000061>
- Ghodpage, R., Patil, P., Gurav, O., Gurubaran, S., & Sharma, A. (2018). Ionospheric response to major storm of 17th march 2015 using multi-instrument data over low latitude station Kolhapur (16.8 N, 74.2 E, 10.6 dip. Lat.). *Advances in Space Research*, 62(3), 624–637. <https://doi.org/10.1016/j.asr.2018.05.003>
- Haerendel, G., & Eccles, J. (1992). The role of the equatorial electrojet in the evening ionosphere. *Journal of Geophysical Research*, 97(A2), 1181–1192. <https://doi.org/10.1029/91ja02227>
- Hashimoto, K. K., Kikuchi, T., Tomizawa, I., Hosokawa, K., Chum, J., Buresova, D., et al. (2020). Penetration electric fields observed at middle and low latitudes during the 22 June 2015 geomagnetic storm. *Earth Planets and Space*, 72(1), 1–15. <https://doi.org/10.1186/s40623-020-01196-0>
- Heelis, R., Lowell, J. K., & Spiro, R. W. (1982). A model of the high-latitude ionospheric convection pattern. *Journal of Geophysical Research*, 87(A8), 6339–6345. <https://doi.org/10.1029/ja087ia08p06339>
- Hocke, K., & Schlegel, K. (1996). A review of atmospheric gravity waves and travelling ionospheric disturbances: 1982–1995. *Annales Geophysicae*, 14(9), 917.
- Huang, C.-S., Foster, J. C., & Kelley, M. C. (2005). Long-duration penetration of the interplanetary electric field to the low-latitude ionosphere during the main phase of magnetic storms. *Journal of Geophysical Research*, 110(A11), A11309. <https://doi.org/10.1029/2005ja011202>
- Huang, C.-S., Sazykin, S., Chau, J. L., Maruyama, N., & Kelley, M. C. (2007). Penetration electric fields: Efficiency and characteristic time scale. *Journal of Atmospheric and Solar-Terrestrial Physics*, 69(10–11), 1135–1146. <https://doi.org/10.1016/j.jastp.2006.08.016>
- Huang, F., Lei, J., Xiong, C., Zhong, J., & Li, G. (2021). Observations of equatorial plasma bubbles during the geomagnetic storm of October 2016. *Earth and Planetary Physics*, 5(5), 416–426. <https://doi.org/10.26464/ep2021043>
- Karan, D. K., Daniell, R. E., England, S. L., Martinis, C. R., Eastes, R. W., Burns, A. G., & McClintock, W. E. (2020). First zonal drift velocity measurement of equatorial plasma bubbles (EPBS) from a geostationary orbit using gold data. *Journal of Geophysical Research: Space Physics*, 125(9), e2020JA028173. <https://doi.org/10.1029/2020ja028173>
- Karan, D. K., Eastes, R. W., Daniell, R. E., Martinis, C. R., & McClintock, W. E. (2023). Gold mission's observation about the geomagnetic storm effects on the nighttime equatorial ionization anomaly (EIA) and equatorial plasma bubbles (EPB) during a solar minimum equinox. *Space Weather*, 21(3), e2022SW003321. <https://doi.org/10.1029/2022sw003321>
- Kelley, M. C. (2009). *The Earth's ionosphere: Plasma physics and electrodynamics*. Academic press.
- Kil, H. (2015). The morphology of equatorial plasma bubbles—a review. *Journal of Astronomy and Space Sciences*, 32(1), 13–19. <https://doi.org/10.5140/jass.2015.32.1.13>
- Klimenko, M., & Klimenko, V. (2012). Disturbance dynamo, prompt penetration electric field and overshielding in the earth's ionosphere during geomagnetic storm. *Journal of Atmospheric and Solar-Terrestrial Physics*, 90, 146–155. <https://doi.org/10.1016/j.jastp.2012.02.018>
- Lissa, D., Srinivasu, V., Prasad, D., & Niranjan, K. (2020). Ionospheric response to the 26 August 2018 geomagnetic storm using gps-tec observations along 80 E and 120 E longitudes in the asian sector. *Advances in Space Research*, 66(6), 1427–1440. <https://doi.org/10.1016/j.asr.2020.05.025>
- Martinis, C., Daniell, R., Eastes, R., Norrell, J., Smith, J., Klenzing, J., et al. (2021). Longitudinal variation of postsunset plasma depletions from the global-scale observations of the limb and disk (GOLD) mission. *Journal of Geophysical Research: Space Physics*, 126(2), e2020JA028510. <https://doi.org/10.1029/2020ja028510>
- Martinis, C., Mendillo, M., & Aarons, J. (2005). Toward a synthesis of equatorial spread f onset and suppression during geomagnetic storms. *Journal of Geophysical Research*, 110(A7), A07306. <https://doi.org/10.1029/2003ja010362>
- Picanço, G. A. S., Denardini, C. M., Nogueira, P. A. B., Resende, L. C. A., Carmo, C. S., Chen, S. S., et al. (2022). Study of the equatorial and low-latitude total electron content response to plasma bubbles during solar cycle 24–25 over the brazilian region using a disturbance ionosphere index. *Annales Geophysicae*, 40(4), 503–517. <https://doi.org/10.5194/angeo-40-503-2022>
- Qian, L., Burns, A. G., Emery, B. A., Foster, B., Lu, G., Maute, A., et al. (2014). The NCAR TIE-GCM: A community model of the coupled thermosphere/ionosphere system. *Modeling the Ionosphere–Thermosphere System*, 73–83.
- Qian, L., Wang, W., Burns, A. G., Chamberlin, P. C., Coster, A., Zhang, S.-R., & Solomon, S. C. (2019). Solar flare and geomagnetic storm effects on the thermosphere and ionosphere during 6–11 September 2017. *Journal of Geophysical Research: Space Physics*, 124(3), 2298–2311. <https://doi.org/10.1029/2018ja026175>
- Reinisch, B. W., & Galkin, I. A. (2011). Global ionospheric radio observatory (GIRO). *Earth Planets and Space*, 63(4), 377–381. <https://doi.org/10.5047/eps.2011.03.001>
- Richmond, A., & Fang, T.-W. (2015). Electrodynamics of the equatorial evening ionosphere: 2. Conductivity influences on convection, current, and electrodynamic energy flow. *Journal of Geophysical Research: Space Physics*, 120(3), 2133–2147. <https://doi.org/10.1002/2014ja020935>

- Rienecker, M. M., Suarez, M. J., Gelaro, R., Todling, R., Bacmeister, J., Liu, E., et al. (2011). MERRA: NASA's modern-era retrospective analysis for research and applications. *Journal of Climate*, *24*(14), 3624–3648. <https://doi.org/10.1175/jcli-d-11-00015.1>
- Santos, A., Abdu, M., Sobral, J., Koga, D., Nogueira, P., & Candido, C. (2012). Strong longitudinal difference in ionospheric responses over Fortaleza (Brazil) and Jicamarca (Peru) during the January 2005 magnetic storm, dominated by northward IMF. *Journal of Geophysical Research*, *117*(A8), A08333. <https://doi.org/10.1029/2012ja017604>
- Sousasantos, J., Gomez Socola, J., Rodrigues, F. S., Eastes, R. W., Brum, C. G., & Terra, P. (2023). Severe I-band scintillation over low-to-mid latitudes caused by an extreme equatorial plasma bubble: Joint observations from ground-based monitors and gold. *Earth Planets and Space*, *75*(1), 1–12. <https://doi.org/10.1186/s40623-023-01797-5>
- Sripathi, S., Abdu, M., Patra, A., & Ghodpage, R. (2018). Unusual generation of localized EPB in the dawn sector triggered by a moderate geomagnetic storm. *Journal of Geophysical Research: Space Physics*, *123*(11), 9697–9710. <https://doi.org/10.1029/2018ja025642>
- Sultan, P. (1996). Linear theory and modeling of the Rayleigh-Taylor instability leading to the occurrence of equatorial spread F. *Journal of Geophysical Research*, *101*(A12), 26875–26891. <https://doi.org/10.1029/96ja00682>
- Tsunoda, R. T. (2015). Upwelling: A unit of disturbance in equatorial spread f. *Progress in Earth and Planetary Science*, *2*(1), 1–14. <https://doi.org/10.1186/s40645-015-0038-5>
- Wan, X., Zhong, J., Zhang, S.-R., Xiong, C., Wang, H., Liu, Y., et al. (2022). Disturbance neutral winds effects on the ionospheric strip-like bulge at lower-middle latitudes. *Journal of Geophysical Research: Space Physics*, *127*(8), e2022JA030541. <https://doi.org/10.1029/2022ja030541>
- Wei, Y., Zhao, B., Li, G., & Wan, W. (2015). Electric field penetration into earth's ionosphere: A brief review for 2000–2013. *Science Bulletin*, *60*(8), 748–761. <https://doi.org/10.1007/s11434-015-0749-4>
- Weimer, D. (2005). Improved ionospheric electrodynamic models and application to calculating joule heating rates. *Journal of Geophysical Research*, *110*(A5), A05306. <https://doi.org/10.1029/2004ja010884>
- Wu, K., Xu, J., Yue, X., Xiong, C., Wang, W., Yuan, W., et al. (2020). Equatorial plasma bubbles developing around sunrise observed by an all-sky imager and global navigation satellite system network during storm time. *Annales Geophysicae*, *38*(1), 163–177. <https://doi.org/10.5194/angeo-38-163-2020>
- Xiong, C., Lühr, H., & Fejer, B. G. (2016). The response of equatorial electrojet, vertical plasma drift, and thermospheric zonal wind to enhanced solar wind input. *Journal of Geophysical Research: Space Physics*, *121*(6), 5653–5663. <https://doi.org/10.1002/2015ja022133>
- Zakharenkova, I., Cherniak, I., & Krankowski, A. (2019). Features of storm-induced ionospheric irregularities from ground-based and spaceborne GPS observations during the 2015 St. Patrick's Day storm. *Journal of Geophysical Research: Space Physics*, *124*(12), 10728–10748. <https://doi.org/10.1029/2019ja026782>